

## PAPER

[View Article Online](#)  
[View Journal](#) | [View Issue](#)Cite this: *Nanoscale Adv.*, 2020, 2, 3963

# Cobalt and nitrogen codoped carbon nanotubes derived from a graphitic C<sub>3</sub>N<sub>4</sub> template as an electrocatalyst for the oxygen reduction reaction†

Jichang Zhang,<sup>a</sup> Chenxia Li,<sup>b</sup> Ming Zhang,<sup>a</sup> Jianqi Zhang,<sup>a</sup> Xi Wu,<sup>a</sup> Xuesong Li<sup>\*b</sup> and Wei Lü<sup>ID</sup> <sup>\*b</sup>

Sluggish oxygen reduction reaction kinetics have been a main obstacle for commercial application of fuel cells. To replace Pt-based noble metal electrocatalysts, it is crucial to develop economical materials as electrocatalysts. Herein, we provide a strategy to prepare Co and N codoped carbon nanotubes for efficient oxygen reduction reaction. The composites are synthesized by hydrothermal reaction followed by calcination at 900 °C. Graphitic carbon nitride is used as a template and nitrogen source, and citric acid and cobalt nitrate hexahydrate are used as carbon and cobalt sources, respectively. Due to the synergistic effect of Co and N codoping and increased specific surface area, the resulting Co and N codoped carbon nanotubes exhibit excellent catalytic performance. The present results provide experimental support for further development of electrocatalysts.

Received 19th June 2020

Accepted 30th July 2020

DOI: 10.1039/d0na00502a

[rsc.li/nanoscale-advances](http://rsc.li/nanoscale-advances)

## 1. Introduction

The increasing energy demand and the impact of traditional energy on the environment highlight the need to pursue clean and renewable energy supply.<sup>1,2</sup> An environmentally friendly solution is fuel cell technology, which provides clean and sustainable electricity.<sup>3,4</sup> But the sluggish oxygen reduction reaction (ORR) kinetics at the cathode of a fuel cell limits its commercial application. Traditionally, platinum (Pt) has been considered as the best ORR catalyst.<sup>5,6</sup> However, Pt is expensive and prone to methanol poisoning when used as an ORR catalyst. Therefore, the development of an environmentally friendly, efficient and stable catalyst to replace Pt-based catalysts has become an urgent need.<sup>7–9</sup>

Currently, metal-free nitrogen-doped carbon materials are popular materials for research globally. As some of ORR's most promising non-noble metal catalysts, they have good catalytic activity, low cost, high stability and environmental friendliness.<sup>10–14</sup> Furthermore, N-doped carbon materials have received great attention due to their simple preparation methods and structural characteristics. The introduction of N atoms in carbon materials could significantly enhance electrocatalytic

activity, thus inducing efficient ORR.<sup>15–17</sup> In addition, previous reports have indicated that doping carbon materials with transition metals such as Co, Fe, Ni, *etc.* is also an effective way to improve the catalytic performance of the catalyst.<sup>18–22</sup> In spite of the great efforts dedicated to ORR research, obtaining effective ORR catalytic materials comparable to the commercial Pt/C catalyst remains a challenge.

From the above discussion, it can be deduced that it is possible to develop a transition metal and N codoped material system for efficient ORR, and several groups have reported related results.<sup>23–28</sup> g-C<sub>3</sub>N<sub>4</sub> is a typical two-dimensional (2D) conjugated polymer material. As a cheap, non-metal, visible light-responsive photocatalyst, it has attracted widespread attention in terms of electrochemistry.<sup>29,30</sup> It has the advantages of high physical and chemical stability, easy preparation, non-toxicity, abundant raw materials, and high nitrogen content, and has become one of the well-known nitrogen-rich compounds.<sup>31–34</sup> Most importantly, various 2D or 3D structures can be obtained by controlling the synthesis conditions. The synthesis temperature of nitrogen-doped carbon materials is usually higher than 800 °C, which can meet the requirements for template removal.<sup>35,36</sup> Therefore, g-C<sub>3</sub>N<sub>4</sub> containing only carbon and nitrogen elements can be used to synthesize an N-doped carbon material.<sup>37–40</sup> In the present work, we developed a facile method to prepare Co and N codoped carbon nanotubes (CNTs) as electrocatalysts. The composites are synthesized by hydrothermal reaction followed by calcination at 900 °C. Graphitic carbon nitride (g-C<sub>3</sub>N<sub>4</sub>) is used as a template and nitrogen source, and citric acid (CA) and cobalt nitrate hexahydrate are used as the carbon and cobalt sources, respectively. The resulting Co and N codoped CNTs exhibit high specific

<sup>a</sup>Cardiology Department, The Second Hospital of Jilin University, Jilin University, Changchun 130041, China

<sup>b</sup>Key Laboratory of Advanced Structural Materials, Ministry of Education & Advanced Institute of Materials Science, Changchun University of Technology, Changchun 130012, China. E-mail: [lixuesong@ccut.edu.cn](mailto:lixuesong@ccut.edu.cn); [lw771119@hotmail.com](mailto:lw771119@hotmail.com); Fax: +86-431-85716577; Tel: +86-431-85716577

† Electronic supplementary information (ESI) available. See DOI: 10.1039/d0na00502a

surface area ( $523 \text{ m}^2 \text{ g}^{-1}$ ) and high nitrogen content (5.71%), showing excellent ORR activity, durability, and resistance to methanol.

## 2. Experimental

### 2.1 Synthesis of $\text{g-C}_3\text{N}_4$

15 g of urea was placed in a ceramic crucible with a cover, heated to  $550^\circ\text{C}$  and kept at this temperature for 4 h. Then, the product was naturally cooled to room temperature and ground to obtain a bright yellow  $\text{g-C}_3\text{N}_4$  powder.

### 2.2 Synthesis of Co, N-CNT

Typically, 0.5 g  $\text{g-C}_3\text{N}_4$  and 0.1 g  $\text{Co}(\text{NO}_3)_3 \cdot 6\text{H}_2\text{O}$  were added into 20 ml of CA (0.15 M) aqueous solution under ultrasonication for 4 h. Then, the prepared suspension was transferred into a Teflon autoclave and kept at different temperatures ( $100^\circ\text{C}$ ,  $120^\circ\text{C}$ ,  $140^\circ\text{C}$ ,  $160^\circ\text{C}$ , and  $180^\circ\text{C}$ ) for 10 h. The resulting samples were collected by centrifugation, washed and dried at  $60^\circ\text{C}$  overnight, and the samples are denoted as  $\text{g-C}_3\text{N}_4@\text{PCA-T}$  ( $T$  is the hydrothermal temperature). After that,  $\text{g-C}_3\text{N}_4@\text{PCA-T}$  was calcined at  $900^\circ\text{C}$  for 1 h in a nitrogen atmosphere to obtain Co and N codoped CNTs, and the samples with different hydrothermal temperatures are denoted as Co, N-CNT- $T$ , respectively.

## 3. Results and discussion

The synthesis procedure of the Co, N-CNT samples is shown in Fig. 1. CA was used as a carbon source and cobalt nitrate hexahydrate provided the cobalt element. The  $\text{g-C}_3\text{N}_4$  nano-sheets were used as templates and nitrogen sources. There are three reasons for the two-step heat treatment for the synthesis of Co, N-CNTs. Firstly,  $\text{g-C}_3\text{N}_4$  has a hierarchical structure and it could completely disappear after calcination at  $900^\circ\text{C}$ . Secondly, use of CA as a carbon source is mainly due to the wide source of raw materials. The product obtained by chemical reaction of CA with  $\text{g-C}_3\text{N}_4$  can strengthen the connection between the carbon source and nitrogen source. CA could polymerize and cover the calcined  $\text{g-C}_3\text{N}_4$  surface during carbonization. Finally, after high-temperature treatment,  $\text{Co}(\text{NO}_3)_3 \cdot 6\text{H}_2\text{O}$  provides Co atoms and forms a high nitrogen content Co, N-CNT structure, which provides abundant active sites for the ORR.

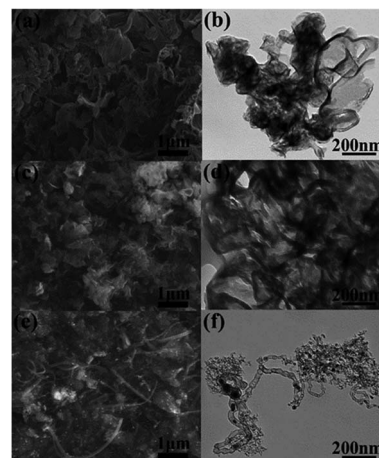


Fig. 2 (a) SEM and (b) TEM images of  $\text{g-C}_3\text{N}_4$ ; (c) SEM and (d) TEM images of  $\text{g-C}_3\text{N}_4@\text{PCA-140}$ ; (e) SEM and (f) TEM images of Co, N-CNT-140.

Fig. 2(a) and (b) show the original  $\text{g-C}_3\text{N}_4$  scanning electron microscope (SEM) and transmission electron microscope (TEM) images, and the lamellar structure of  $\text{g-C}_3\text{N}_4$  can be clearly observed. After adding CA and cobalt nitrate hexahydrate, the hydrothermal treatment was performed at  $140^\circ\text{C}$  to obtain  $\text{g-C}_3\text{N}_4@\text{PCA-140}$  with a sheet-like structure, where  $\text{g-C}_3\text{N}_4$  was coated by PCA. This can be observed from Fig. 2(c) and (d). After high temperature calcination at  $900^\circ\text{C}$ , as shown in Fig. 2(e) and (f), Co, N-CNT-140 with carbon nanotube structures could be acquired. A possible reason for this is that the lamellar structure is transformed into a carbon nanotubular structure during the high-temperature carbonization process and the black part in the transmission image represents cobalt nanoparticles with some layered structures. The SEM and TEM images of  $\text{g-C}_3\text{N}_4@\text{PCA-T}$  and Co, N-CNT- $T$  obtained at other hydrothermal temperatures are shown in Fig. S1 and S2,<sup>†</sup> respectively. It can be seen that at hydrothermal temperatures of  $120^\circ\text{C}$ ,  $140^\circ\text{C}$ , and  $160^\circ\text{C}$ , the sheet structure in  $\text{g-C}_3\text{N}_4@\text{PCA-T}$  can be observed. When hydrothermal treatment was performed at  $180^\circ\text{C}$ , the lamellar structure collapsed into a fragmented structure, which failed to be a lamellar template. After high temperature treatment, for Co, N-CNT-120, a partial CNT structure is acquired. Co, N-CNT-140 exhibits the best CNT morphology. Upon further increasing the hydrothermal temperature, this structure begins to collapse. When it reaches  $180^\circ\text{C}$ , the CNT structure is completely destroyed. This may be

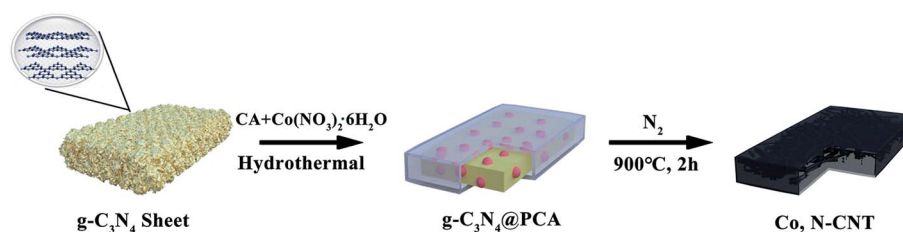


Fig. 1 The synthetic procedure of Co, N-CNT electrocatalysts.



the main reason for the worse catalytic performance with the higher hydrothermal temperature.

Fig. 3(a) shows the XRD curves of Co, N-CNT-*T*. After high-temperature carbonization, a broad graphite-like peak appeared at around  $23.30^\circ$ . In addition, cobalt nitrate hexahydrate was reduced to elemental cobalt after a high temperature treatment at  $900^\circ\text{C}$ , and the standard peaks of cobalt appeared at  $44.32^\circ$ ,  $52.12^\circ$ , and  $76.20^\circ$ , corresponding to (111), (200), and (220) crystal planes, respectively.<sup>41</sup> Compared with the standard map (PDF89-4307),<sup>42</sup> it is  $\alpha$ -Co with a face-centered cubic structure and formed on the surface of CNTs after high-temperature treatment. With increasing hydrothermal temperature, the diffraction peak of Co becomes narrower, and the intensity gradually increases. This indicates that the size of Co crystal grains increases as the temperature increases. This is further confirmed by FT-IR and Raman measurements.

The functional groups existing on the surface of Co, N-CNT-*T* were analyzed by FT-IR spectroscopy. Fig. 3(b) shows the FT-IR spectra of  $\text{g-C}_3\text{N}_4$  and  $\text{g-C}_3\text{N}_4@\text{PCA-T}$ , indicating that these samples include similar carbon and oxygen containing functional groups.<sup>43</sup> The series of peaks in the region of  $1200\text{--}1650\text{ cm}^{-1}$  originate from the typical stretching vibrations of CN heterocycles. The broad bands at  $3200\text{--}3400\text{ cm}^{-1}$  are ascribed to the adsorbed  $\text{H}_2\text{O}$  molecules or the N-H vibration. After high-temperature carbonization, two obvious peaks remain for Co, N-CNT-140 at  $1500\text{--}1700\text{ cm}^{-1}$  and  $2980\text{ cm}^{-1}$  in Fig. 3(c), which are ascribed to the C-C, C=C and C-N vibrations. This shows that high temperature carbonization destroys O-H, N-H and

other chemical bonds, while C-N bonds are relatively stable, thereby ensuring that nitrogen can be effectively doped. For the Raman spectra of Co, N-CNT-*T* in Fig. 3(d), the peaks at  $1350$  and  $1580\text{ cm}^{-1}$  correspond to the D and G bands, respectively.<sup>44</sup> The relative intensity ratio of D and G bands ( $I_D/I_G$ ) decreases from 1.12 to 1.01 with increasing hydrothermal temperature, indicating an increased graphitization degree. The decrease in  $I_D/I_G$  proves that the structures become more ordered. XPS further proves this conclusion in Fig. S3.† The characteristic Raman peak of Co corresponds to a wavelength of about  $680\text{ cm}^{-1}$ ,<sup>45</sup> and the intensity of the peak becomes more obvious as the hydrothermal temperature increases. This is consistent with reports in the literature. At the same time, the doping of Co and N elements changed the surface structure of the material.

The hydrothermal temperature has a great influence on the specific surface area of the material and the structure of the pores. We measured the  $\text{N}_2$  physical adsorption capacity of all samples. The adsorption isotherms of pure  $\text{g-C}_3\text{N}_4$  and Co, N-CNT-*T* ( $120^\circ\text{C}$ ,  $140^\circ\text{C}$ , and  $160^\circ\text{C}$ ) are shown in Fig. 4. According to the classification criteria, it can be seen that the  $\text{N}_2$  adsorption isotherm curves of all samples showed a type IV shape, and the relative pressure appeared near  $p/p_0 = 0.9$ , indicating a mesoporous structure. From the BET curves, it can be concluded that the specific surface areas of  $\text{g-C}_3\text{N}_4$  and Co, N-CNT-*T* ( $120^\circ\text{C}$ ,  $140^\circ\text{C}$ , and  $160^\circ\text{C}$ ) are 85, 480, 523, and  $230\text{ m}^2\text{ g}^{-1}$ , respectively. Co, N-CNT-140 has the largest specific surface area. The inset of the graphs shows the pore size distribution of the samples. Samples of  $\text{g-C}_3\text{N}_4$  and Co, N-CNT-*T* ( $120^\circ\text{C}$ ,

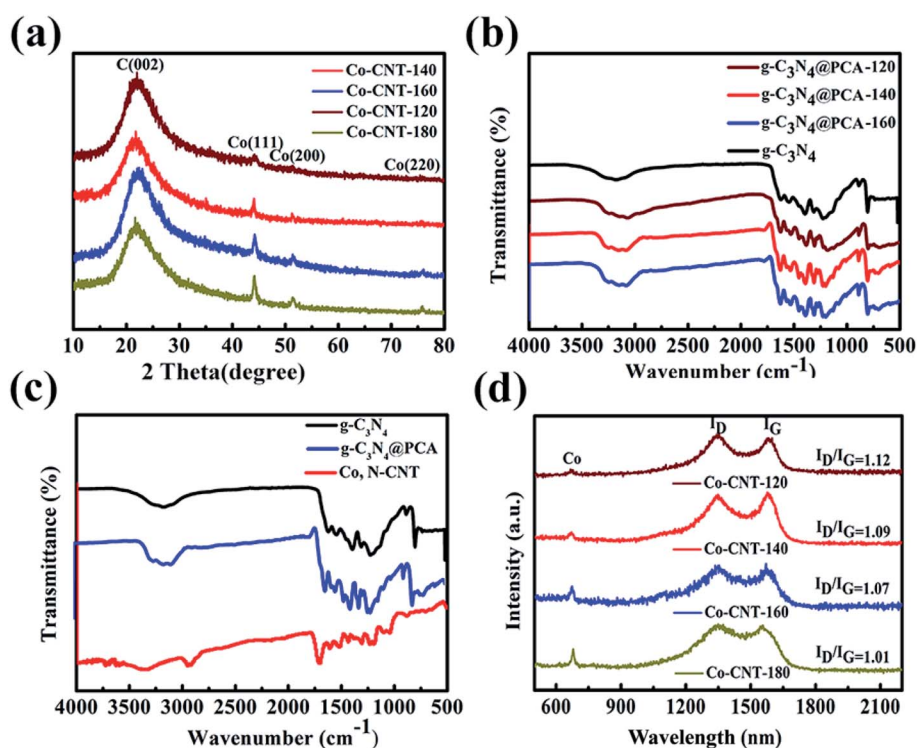


Fig. 3 (a) XRD patterns of Co, N-CNT-*T* ( $120^\circ\text{C}$ ,  $140^\circ\text{C}$ ,  $160^\circ\text{C}$ , and  $180^\circ\text{C}$ ); (b) FT-IR spectra of  $\text{g-C}_3\text{N}_4$ ,  $\text{g-C}_3\text{N}_4@\text{PCA-120}$ ,  $\text{g-C}_3\text{N}_4@\text{PCA-140}$ , and  $\text{g-C}_3\text{N}_4@\text{PCA-160}$ ; (c) FT-IR spectra of  $\text{g-C}_3\text{N}_4$ ,  $\text{g-C}_3\text{N}_4@\text{PCA-140}$ , and Co, N-CNT-140; (d) Raman spectra of Co, N-CNT-*T* ( $120^\circ\text{C}$ ,  $140^\circ\text{C}$ ,  $160^\circ\text{C}$ , and  $180^\circ\text{C}$ ).



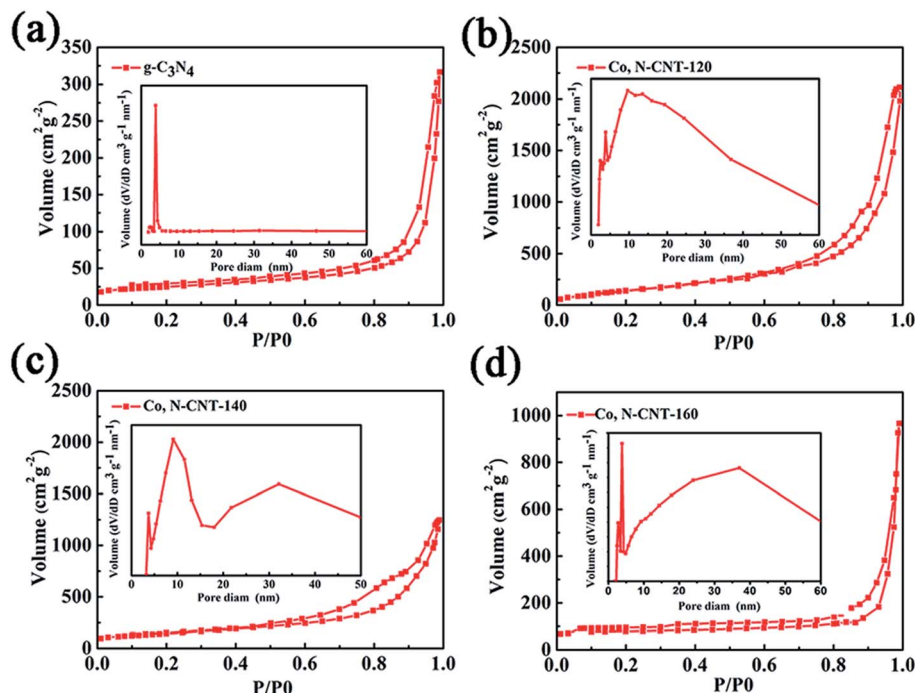


Fig. 4 (a)  $N_2$  adsorption/desorption isotherms of  $g-C_3N_4$ . Inset: pore size distribution of  $g-C_3N_4$ . (b–d)  $N_2$  adsorption/desorption isotherms of Co, N-CNT- $T$  (120 °C, 140 °C, and 160 °C). Inset: pore size distribution of Co, N-CNT- $T$  (120 °C, 140 °C, and 160 °C).

140 °C, and 160 °C) have pore size distributions in the range of micropores and mesopores. Such porous cobalt–nitrogen codoped carbon nanotubes are more favorable for oxygen transmission and further increase the active sites for the ORR. Moreover, a large amount of gas generated during the process of removing the template  $g-C_3N_4$  may introduce additional pore structures, which is beneficial for the ORR.

As shown in Fig. S3,<sup>†</sup> we used XPS to determine the elemental composition of Co, N-CNT- $T$  (120 °C, 140 °C, and 160 °C). The XPS spectrum showed the presence of C1s, N1s, O1s and Co2p XPS peaks in all N-CNT- $T$  samples, which is consistent with the results obtained by XRD. It can be seen from Table 1 that as the hydrothermal temperature increases, the content of carbon atoms decreases, and the content of nitrogen and cobalt increases.

It can be seen from Fig. 5 that the XPS spectra of C1s of all samples can be fitted to four peaks at 284.7 eV, 285.5 eV, 286.1 eV, and 287.1 eV. As shown in Fig. 5(a), (d) and (g), the peak located at about 284.7 eV corresponds to the C=C bond. The peaks with higher binding energies were at 285.5 eV (C–N), 286.1 eV (C–O), and 287.1 eV (C=O). It can be seen that with the

increase of the hydrothermal temperature, the strength of the C=C bond decreases significantly while the strength of C–N and C–O increases significantly. The main reason is that as the hydrothermal temperature increases, the thickness of carbon layer formed due to citric acid carbonization increases slightly, and the carbon nanotube structure is formed by high temperature heat treatment. The corresponding high-resolution N1s spectra are shown in Fig. 5(b), (e) and (h), which confirm the successful doping of N into CNTs. The XPS peaks of N1s are divided into pyridinic-N, pyrrolic-N, graphitic-N, and oxidized-N with the corresponding binding energy positions at 398.7 eV, 399.7 eV, 401 eV, and 403.3 eV, respectively. It can be seen from Table 2 that with increasing hydrothermal temperature, the content of different types of nitrogen increases too. It is worth noting that the main nitrogen states in Co, N-CNT- $T$  are pyridinic-N and graphitic-N, which are recognized as active sites during the ORR and provide good electrical conductivity. Therefore, a high N content is preferred. The high-resolution XPS spectra for Co2p are shown in Fig. 5(c), (f) and (i). The Co2p<sub>1/2</sub> peaks are at 780.6 eV and 796.2 eV (Co2p<sub>1/2</sub>), and those of Co2p<sub>3/2</sub> are at 785.9 eV and 802.6 eV. Co2p<sub>1/2</sub> is produced by the exposed metals Co and Co<sub>x</sub>O<sub>y</sub>, which may be derived from the raw material cobalt nitrate hexahydrate to form elemental Co and Co oxides at high temperatures.<sup>46,47</sup> Co2p<sub>3/2</sub> is attributed to Co–N<sub>x</sub> groups, partly derived from N in the raw materials, and partly due to the heat treatment under an atmosphere of N<sub>2</sub>, forming Co–N<sub>x</sub> groups. After adding Co, the catalytic activity of the product is significantly improved, so Co–N<sub>x</sub> and Co<sub>x</sub>O<sub>y</sub> are expected to be the additional active sites for the ORR.<sup>48,49</sup> This is due to the synergy between metals, metal oxides, metal nitrides,

Table 1 Elemental composition and content of Co, N-CNT- $T$  (120 °C, 140 °C, and 160 °C)

Sample	C [at%]	N [at%]	Co [at%]
Co, N-CNT-120	96.35	3.14	0.51
Co, N-CNT-140	94.35	4.58	1.07
Co, N-CNT-160	87.75	9.81	2.44





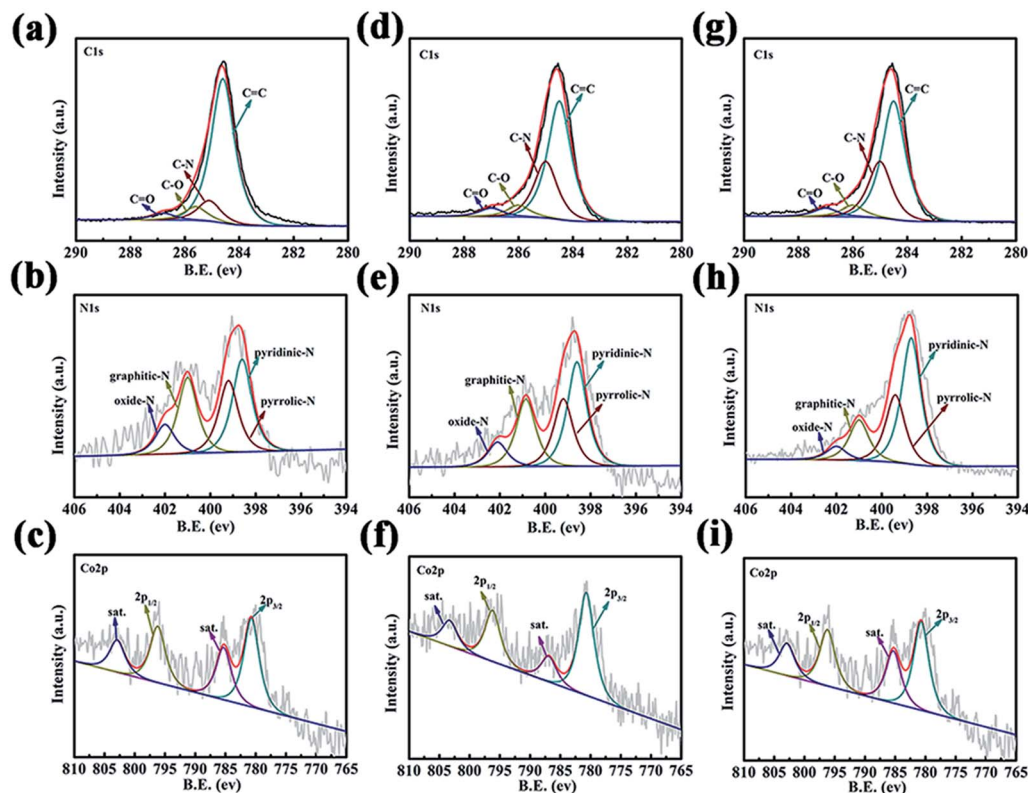


Fig. 5 (a–c) C1s, N1s, and Co2p XPS spectra of Co, N-CNT-120; (d–f) C1s, N1s, and Co2p XPS spectra of Co, N-CNT-140; (g–i) C1s, N1s, and Co2p XPS spectra of Co, N-CNT-160.

Table 2 Content of different types of nitrogen in Co, N-CNT-*T* (120 °C, 140 °C, and 160 °C)

Sample	N [at%]	Pyridinic-N [at%]	Pyrrolic-N [at%]	Graphitic-N [at%]	Oxidized-N [at%]
Co, N-CNT-120	3.14	1.06	0.80	0.90	0.34
Co, N-CNT-140	4.58	1.81	1.17	1.17	0.42
Co, N-CNT-160	9.81	5.00	2.70	1.60	0.53

*etc.* and CNTs. With increasing hydrothermal temperature, the intensity of the Co peaks in the different samples increased, which is consistent with the results of XRD.

The CV curve of Co, N-CNT-140 is shown in Fig. 6(a). By comparing the N<sub>2</sub> atmosphere and the O<sub>2</sub> atmosphere, it can be deduced that Co, N-CNT-140 does not show a significant oxygen reduction peak under the nitrogen atmosphere. The oxygen reduction peak of Co, N-CNT-140 shows a rectangular shape. It indicates that the material has very good conductivity and excellent capacitance current. Under oxygen conditions, a significant CV peak was observed due to the oxygen reduction reaction, and the voltage relative to RHE is 0.801 V. In Fig. 6(b) and S4,† we further verify the stability of the material. After adding 3 M methanol solution, the oxygen reduction peak of the material does not change significantly, which indicates that Co, N-CNT-140 has good methanol resistance. The CV curves at different hydrothermal temperatures are shown in Fig. 6(c) and S5.† Clear oxygen reduction peaks were observed for all Co, N-

CNT-*T* samples, and the voltages relative to RHE are 0.736 V (Co, N-CNT-120), 0.815 V (Co, N-CNT-140), 0.836 V (Co, N-CNT-160), and 0.723 V (Co, N-CNT-180), respectively. As the hydrothermal temperature increases from 120 to 140 °C, the position of the reduction peak moves closer to that of the Pt/C catalyst, but the catalytic performance begins to decrease with further increasing the hydrothermal temperature to 160 and 180 °C. The most likely reason is that the structure of carbon nanotubes is destroyed with increasing hydrothermal temperature. At 180 °C, the structure of carbon nanotubes is completely destroyed and fragmented to small layer structures. This structure may cause the material to have poor conductivity and few active sites, which is not conducive to the progress of the ORR.

To further determine the kinetics of the ORR, we used a rotating disk electrode (RDE) to characterize Co, N-CNT-*T* in O<sub>2</sub> saturated 0.1 M KOH, and compared it with commercial Pt/C. It can be seen from Fig. 6(e) that as the rotation speed



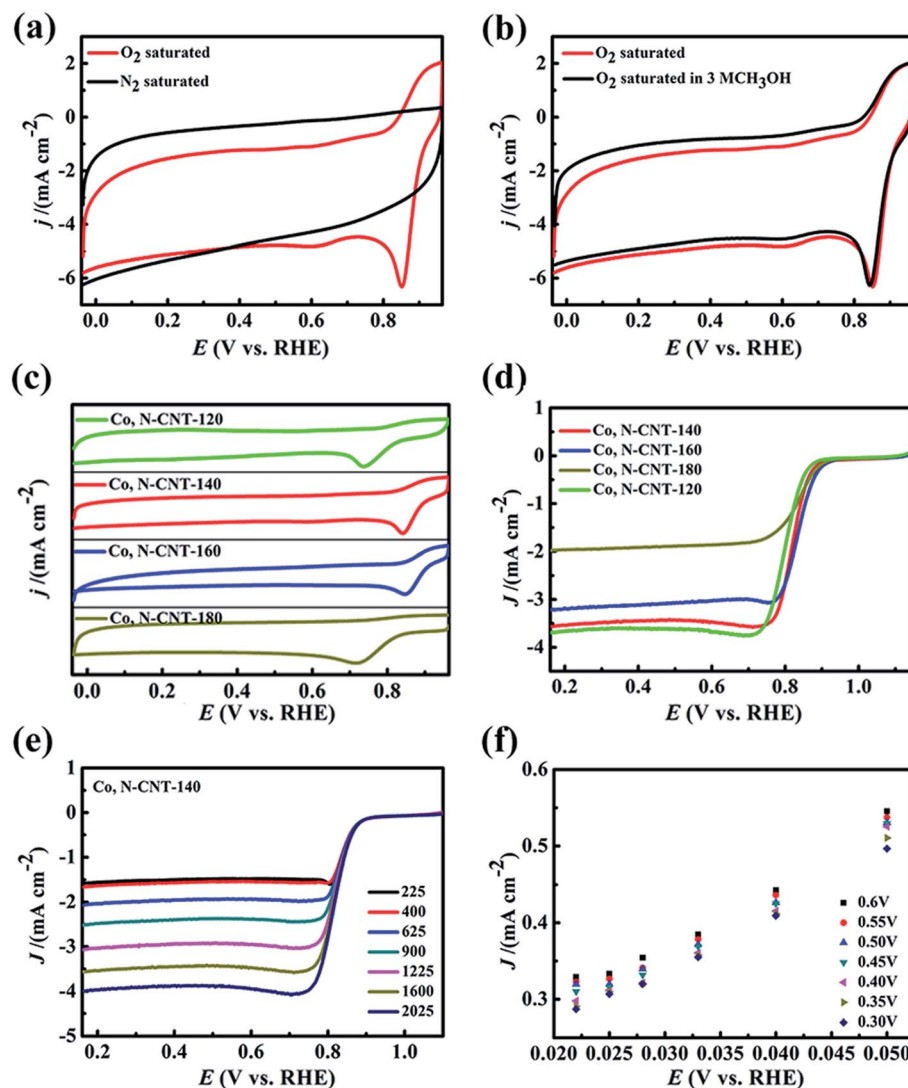


Fig. 6 (a) CV curves of Co, N-CNT-140 in  $N_2$  and  $O_2$  saturated 0.1 M KOH aqueous solution with a scan rate of  $100 \text{ mV s}^{-1}$ . (b) CV of Co, N-CNT-140 in  $O_2$ -saturated 0.1 M KOH solution with 3 M  $CH_3OH$ . (c) CV curves of Co, N-CNT- $T$  (120  $^{\circ}C$ , 140  $^{\circ}C$ , 160  $^{\circ}C$ , and 180  $^{\circ}C$ ) in  $O_2$  saturated 0.1 M KOH aqueous solution with a scan rate of  $100 \text{ mV s}^{-1}$ . (d) LSV curves of Co, N-CNT- $T$  (120  $^{\circ}C$ , 140  $^{\circ}C$ , 160  $^{\circ}C$ , and 180  $^{\circ}C$ ) at 1600 rpm rotating speeds. (e) LSV curves using a rotating-disk electrode; (f) number of transferred electrons of Co, N-CNT-140 at different potentials.

increases, the limiting current density increases continuously. Therefore, we chose a stable speed of 1600 rpm to determine the initial voltage, half-peak voltage and limiting current density of the sample, and the results of the other samples are shown in Fig. S6<sup>†</sup>. It can be deduced that the initial voltages of Co, N-CNT-120, Co, N-CNT-140, Co, N-CNT-160, and Co, N-CNT-180 samples were 0.874, 0.877, 0.868 and 0.844 V, respectively. The limiting current densities for the ORR were 3.55, 3.57, 3.13, and 1.97  $\text{mA cm}^{-2}$ , respectively. This trend can also be determined from the half-peak voltages (0.814, 0.830, 0.868 and 0.789 V, respectively).

By comparison, it can be concluded that Co, N-CNT-140 shows the best performance in terms of limiting current density, half-peak voltage, and cycling stability (Fig. S7 and S8<sup>†</sup>). The ORR theoretically proceeds by two processes ( $4e^-$  and  $2e^-$ ), so we further studied the number of transferred electrons of Co,

N-CNT-140. The K-L curve can be obtained by analyzing the LSV curve, and the number of transferred electrons in the sample can be further determined. Fig. 6(f) shows that the K-L curve of Co, N-CNT-140 has an obvious linear relationship. The calculated number of transferred electrons of the sample is 3.91 and corresponds to a four-electron process of the ORR. At the same time, in order to explore the effect of different hydrothermal temperatures on the performance of the catalyst, we performed linear scan voltammetry curve and K-L curve analysis of samples at different temperatures as shown in Fig. S4<sup>†</sup>. It can be seen from Fig. S4(a), (c) and (e)<sup>†</sup> that the limiting current density of the samples at different temperatures increases with the increase of the rotation speed. The number of electrons transferred from Co, N-CNT-120, Co, N-CNT-160, and Co, N-CNT-180 in Fig. S4(b), (d) and (f)<sup>†</sup> is 2.5, 4.7, and 2.6, respectively. It can be seen that the electrocatalysis behavior of



Co, N-CNT-140 is a typical four-electron reaction. The samples obtained at other hydrothermal temperatures are mixed processes of two electrons and four electrons in the catalytic reaction. This is consistent with the results of the CV test. The main reason is that Co, N-CNT-140 has a carbon nanotube structure. This structure provides a large specific surface area with high pyridinic nitrogen content, which may provide a larger contact area and more active sites for the oxygen reaction, thereby accelerating the reaction process. The performance of the catalyst requires not only a correct reduction potential, but also good stability. It can be seen from Fig. S5(a)–(c)† that the peak of the CV curve of each sample does not change significantly after the addition of methanol. This shows that Co, N-CNT-*T* has good methanol resistance and excellent stability. Co, N-CNT-140 exhibits catalytic properties comparable to those of Pt/C catalysts, and it is more tolerant to methanol than Pt/C.

## 4. Conclusion

In summary, we synthesized Co, N-CNT-*T* by a facile two-step method. First, the precursor of g-C<sub>3</sub>N<sub>4</sub>@PCA was hydrothermally synthesized, and then Co, N-CNT was obtained by high temperature heat treatment at 900 °C in a N<sub>2</sub> atmosphere. The good catalytic performance of the Co, N-CNT composite materials in alkaline media is mainly due to the following aspects: firstly, CNT structures are formed, which helps to increase the specific surface area of the material. Secondly, the addition of Co element provides more active sites for the ORR. Finally, after the high temperature treatment, the content of pyridinic nitrogen and graphitic nitrogen increases, which is more helpful for the 4e<sup>−</sup> process with catalytic reaction. This experimental result helps us to design a desired structure in the reaction process without using the existing framework directly, and obtain an ORR catalyst with more excellent performance. At the same time, it also helps us use the same method to obtain catalysts with similar structures.

## Conflicts of interest

There are no conflicts to declare.

## Acknowledgements

This work was financially supported by the National Natural Science Foundation of China (Grant No. 61574021), Science Foundation of Jilin Education Department (Grant No. JJKH20200661KJ and JJKH20201097KJ), and Capital Construction funds within the provincial budget (Grant No. 2019C046-8 and 2019C045-6).

## References

- 1 K. Gong, F. Du, Z. Xia, M. Durstock and L. J. s. Dai, Nitrogen-doped carbon nanotube arrays with high electrocatalytic activity for oxygen reduction, *Science*, 2009, **323**(5915), 760–763.
- 2 V. B. Oliveira, M. Simões, L. F. Melo and A. M. F. R. Pinto, Overview on the developments of microbial fuel cells, *Biochem. Eng. J.*, 2013, **73**(8), 53–64.
- 3 T. Palaniselvam, V. Kashyap, S. N. Bhange, J.-B. Baek and S. Kurungot, Nanoporous Graphene Enriched with Fe/Co-N Active Sites as a Promising Oxygen Reduction Electrocatalyst for Anion Exchange Membrane Fuel Cells, *Adv. Funct. Mater.*, 2016, **26**(13), 2150–2162.
- 4 B. Ni, C. Ouyang, X. Xu, J. Zhuang and X. Wang, Modifying Commercial Carbon with Trace Amounts of ZIF to Prepare Derivatives with Superior ORR Activities, *Adv. Mater.*, 2017, **29**(27), 1701354.
- 5 G. f. Long, X. h. Li, K. Wan, Z. x. Liang, J. h. Piao and P. Tsiakaras, Pt/C N-doped electrocatalysts: Superior electrocatalytic activity for methanol oxidation reaction and mechanistic insight into interfacial enhancement, *Appl. Catal., B*, 2017, **203**, 541–548.
- 6 S. Dai, J. P. Chou, K. W. Wang, Y. Y. Hsu, A. Hu, X. Pan and T. Y. Chen, Platinum-trimer decorated cobalt-palladium core-shell nanocatalyst with promising performance for oxygen reduction reaction, *Nat. Commun.*, 2019, **10**(1), 440.
- 7 J. Zhang, K. Sasaki, E. Sutter and R. J. S. Adzic, Stabilization of platinum oxygen-reduction electrocatalysts using gold clusters, *Science*, 2007, **315**(5809), 220–222.
- 8 C. Chen, Y. Kang, Z. Huo, Z. Zhu, W. Huang, H. L. Xin, J. D. Snyder, D. Li, J. A. Herron and M. J. S. Mavrikakis, Highly crystalline multimetallic nanoframes with three-dimensional electrocatalytic surfaces, *Science*, 2014, **343**(6177), 1339–1343.
- 9 M. L. Pegis, C. F. Wise, D. J. Martin and J. M. Mayer, Oxygen Reduction by Homogeneous Molecular Catalysts and Electrocatalysts, *Chem. Rev.*, 2014, **343**(6177), 1339–1343.
- 10 L. Dai, Y. Xue, L. Qu, H. J. Choi and J. B. Baek, Metal-free catalysts for oxygen reduction reaction, *Chem. Rev.*, 2015, **115**(11), 4823–4892.
- 11 X. Wang, X. Chen, A. Thomas, X. Fu and M. Antonietti, Metal-Containing Carbon Nitride Compounds: A New Functional Organic-Metal Hybrid Material, *Adv. Mater.*, 2009, **21**(16), 1609–1612.
- 12 X. Wang, K. Maeda, A. Thomas, K. Takanabe, G. Xin, J. M. Carlsson, K. Domen and M. Antonietti, A metal-free polymeric photocatalyst for hydrogen production from water under visible light, *Nat. Mater.*, 2009, **8**(1), 76.
- 13 S. Fu, C. Zhu, D. Su, J. Song, S. Yao, S. Feng, M. H. Engelhard, D. Du and Y. Lin, Porous Carbon-Hosted Atomically Dispersed Iron-Nitrogen Moiety as Enhanced Electrocatalysts for Oxygen Reduction Reaction in a Wide Range of pH, *Small*, 2018, **14**(12), e1703118.
- 14 H. Jiang, J. Gu, X. Zheng, M. Liu, X. Qiu, L. Wang, W. Li, Z. Chen, X. Ji and J. Li, Defect-rich and ultrathin N doped carbon nanosheets as advanced trifunctional metal-free electrocatalysts for the ORR, OER and HER, *Energy Environ. Sci.*, 2019, **12**(1), 322–333.
- 15 Y. D. Qu, Z. W. i. Tang, L. F. Duan, X. S. Li, X. Y. Zhang and W. Lü, Synthesis of Three Dimensional Porous Carbon Materials Using g-C<sub>3</sub>N<sub>4</sub> as Template for Supercapacitors, *J. Electrochem. Soc.*, 2019, **166**(15), A3564–A3569.



- 16 I. S. Amiinu, X. Liu, Z. Pu, W. Li, Q. Li, J. Zhang, H. Tang, H. Zhang and S. Mu, From 3D ZIF Nanocrystals to Co-Nx/C Nanorod Array Electrocatalysts for ORR, OER, and Zn-Air Batteries, *Adv. Funct. Mater.*, 2018, **28**(5), 1704638.
- 17 L. Duan, L. Zhao, H. Cong, X. Zhang, W. Lu and C. Xue, Plasma Treatment for Nitrogen-Doped 3D Graphene Framework by a Conductive Matrix with Sulfur for High-Performance Li-S Batteries, *Small*, 2019, **15**(7), e1804347.
- 18 J. Liang, R. F. Zhou, X. M. Chen, Y. H. Tang and S. Z. Qiao, Fe-N decorated hybrids of CNTs grown on hierarchically porous carbon for high-performance oxygen reduction, *Adv. Mater.*, 2014, **26**(35), 6074–6079.
- 19 Z. Y. Song, X. Y. Zhang, X. S. Li, L. F. Duan and W. Lü, Flexible and Stretchable Energy Storage Device Based on Ni(HCO<sub>3</sub>)<sub>2</sub> Nanosheet Decorated Carbon Nanotube Electrodes for Capacitive Sensor, *J. Electrochem. Soc.*, 2019, **166**(16), A4014–A4019.
- 20 Y. Zan, Z. Zhang, H. Liu, M. Dou and F. Wang, Nitrogen and phosphorus co-doped hierarchically porous carbons derived from cattle bones as efficient metal-free electrocatalysts for the oxygen reduction reaction, *J. Mater. Chem. A*, 2017, **5**(46), 24329–24334.
- 21 Q. Li, W. Chen, H. Xiao, Y. Gong, Z. Li, L. Zheng, X. Zheng, W. Yan, W. C. Cheong, R. Shen, N. Fu, L. Gu, Z. Zhuang, C. Chen, D. Wang, Q. Peng, J. Li and Y. Li, Fe Isolated Single Atoms on S, N Codoped Carbon by Copolymer Pyrolysis Strategy for Highly Efficient Oxygen Reduction Reaction, *Adv. Mater.*, 2018, **30**(25), e1800588.
- 22 M. Kominiaik, A. Roguska, W. Nogala, *et al.*, Patterning Cu nanostructures tailored for CO<sub>2</sub> reduction to electrooxidizable fuels and oxygen reduction in alkaline media, *Nanoscale Adv.*, 2019, **1**(7), 2645–2653.
- 23 Z. Chen, L. Cai, X. Yang, C. Kronawitter, L. Guo, S. Shen and B. E. Koel, Reversible Structural Evolution of NiCoOxHy during the Oxygen Evolution Reaction and Identification of the Catalytically Active Phase, *ACS Catal.*, 2018, **8**(2), 1238–1247.
- 24 Y. Jiang, Y.-P. Deng, J. Fu, D. U. Lee, R. Liang, Z. P. Cano, Y. Liu, Z. Bai, S. Hwang, L. Yang, D. Su, W. Chu and Z. Chen, Interpenetrating Triphase Cobalt-Based Nanocomposites as Efficient Bifunctional Oxygen Electrocatalysts for Long-Lasting Rechargeable Zn-Air Batteries, *Adv. Energy Mater.*, 2018, **8**(15), 1702900.
- 25 T. Liu, F. Yang, G. Cheng and W. Luo, Reduced Graphene Oxide-Wrapped Co<sub>9-x</sub> Fe<sub>x</sub>S<sub>8</sub>/Co, Fe-N-C Composite as Bifunctional Electrocatalyst for Oxygen Reduction and Evolution, *Small*, 2018, **14**(10), 1703748.
- 26 H. Zhang, X. Qiu, Y. Chen, S. Wang, S. E. Skrabalak and Y. Tang, Shape Control of Monodispersed Sub-5 nm Pd Tetrahedrons and Lacinate Pd Nanourchins by Maneuvering the Dispersed State of Additives for Boosting ORR Performance, *Small*, 2020, **16**(6), e1906026.
- 27 Y. Jia, X. Sun, Z. Shi, K. Jiang, H. Liu, J. Ben and D. Li, Modulating the Surface State of SiC to Control Carrier Transport in Graphene/SiC, *Small*, 2018, **14**(26), e1801273.
- 28 W. Sun, L. Du, Q. Tan, J. Zhou, Y. Hu, C. Du, Y. Gao and G. Yin, Engineering of Nitrogen Coordinated Single Cobalt Atom Moieties for Oxygen Electroreduction, *ACS Appl. Mater. Interfaces*, 2019, **11**(44), 41258–41266.
- 29 S. Cao, J. Low, J. Yu and M. Jaroniec, Polymeric photocatalysts based on graphitic carbon nitride, *Adv. Mater.*, 2015, **27**(13), 2150–2176.
- 30 W. J. Ong, L. L. Tan, Y. H. Ng, S. T. Yong and S. P. Chai, Graphitic carbon nitride (g-C<sub>3</sub>N<sub>4</sub>)-based photocatalysts for artificial photosynthesis and environmental remediation: Are we a step closer to achieving sustainability?, *Chem. Rev.*, 2016, **116**(12), 7159–7329.
- 31 Z. Liang, B. Sun, X. Xu, H. Cui and J. Tian, Metallic 1T-phase MoS<sub>2</sub> quantum dots/g-C<sub>3</sub>N<sub>4</sub> heterojunctions for enhanced photocatalytic hydrogen evolution, *Nanoscale*, 2019, **11**(25), 12266–12274.
- 32 X. Qian, X. Meng, J. Sun, L. Jiang, Y. Wang, J. Zhang, X. Hu, M. Shalom and J. Zhu, Salt-Assisted Synthesis of 3D Porous g-C<sub>3</sub>N<sub>4</sub> as a Bifunctional Photo- and Electrocatalyst, *ACS Appl. Mater. Interfaces*, 2019, **11**(30), 27226–27232.
- 33 J. Xue, T. Ma, Q. Shen, R. Guan, H. Jia, X. Liu and B. Xu, A novel synthesis method for Ag/g-C<sub>3</sub>N<sub>4</sub> nanocomposite and mechanism of enhanced visible-light photocatalytic activity, *J. Mater. Sci.: Mater. Electron.*, 2019, **30**(16), 15636–15645.
- 34 T. Sun, P. Zhang, W. Chen, K. Wang, X. Fu, T. Zheng and J. Jiang, Single iron atoms coordinated to g-C<sub>3</sub>N<sub>4</sub> on hierarchical porous N-doped carbon polyhedra as a high-performance electrocatalyst for the oxygen reduction reaction, *Chem. Commun.*, 2020, **56**(5), 798–801.
- 35 J. Li, Y. Zhang, X. Zhang, J. Han, Y. Wang, L. Gu, Z. Zhang, X. Wang, J. Jian, P. Xu and B. Song, Direct Transformation from Graphitic C<sub>3</sub>N<sub>4</sub> to Nitrogen-Doped Graphene: An Efficient Metal-Free Electrocatalyst for Oxygen Reduction Reaction, *ACS Appl. Mater. Interfaces*, 2015, **7**(35), 19626–19634.
- 36 H. Yu, L. Shang, T. Bian, R. Shi, G. I. N. Waterhouse, Y. Zhao, C. Zhou, L. Z. Wu, C. H. Tung and T. Zhang, Nitrogen-doped porous carbon nanosheets templated from g-C<sub>3</sub>N<sub>4</sub> as metal-free electrocatalysts for efficient oxygen reduction reaction, *Adv. Mater.*, 2016, **28**(25), 5080–5086.
- 37 O. Naumov, S. Naumov, B. Abel and A. Varga, The stability limits of highly active nitrogen doped carbon ORR nanocatalysts: a mechanistic study of degradation reactions, *Nanoscale*, 2018, **10**(14), 6724–6733.
- 38 S. Lee, Y.-W. Lee, D.-H. Kwak, J.-Y. Lee, S.-B. Han, J. I. Sohn and K.-W. Park, Three-dimensional porous metal–nitrogen doped carbon nanostructure as a superior non-precious electrocatalyst in oxygen reduction reaction, *J. Ind. Eng. Chem.*, 2016, **43**, 170–176.
- 39 Q. Xiang, Y. Liu, X. Zou, B. Hu, Y. Qiang, D. Yu, W. Yin and C. Chen, Hydrothermal Synthesis of a New Kind of N-Doped Graphene Gel-like Hybrid As an Enhanced ORR Electrocatalyst, *ACS Appl. Mater. Interfaces*, 2018, **10**(13), 10842–10850.
- 40 C. Li, X. Li, X. Sun, X. Zhang, L. Duan, X. Yang, L. Wang and W. Lu, Porous Carbon Networks Derived From Graphitic Carbon Nitride for Efficient Oxygen Reduction Reaction, *Nanoscale Res. Lett.*, 2019, **14**(1), 249.





- 41 J. Guo, S. Gadipelli, Y. Yang, Z. Li, Y. Lu, D. J. L. Brett and Z. Guo, An efficient carbon-based ORR catalyst from low-temperature etching of ZIF-67 with ultra-small cobalt nanoparticles and high yield, *J. Mater. Chem. A*, 2019, **7**(8), 3544–3551.
- 42 A. B. A. A. Nassr, T. Kottakkat and M. Bron, A simple microwave process for the preparation of cobalt oxide nanoparticles supported on carbon nanotubes for electrocatalytic applications, *J. Solid State Electrochem.*, 2019, **24**(1), 131–136.
- 43 Z. Chen, S. Lu, Q. Wu, F. He, N. Zhao, C. He and C. Shi, Salt-assisted synthesis of 3D open porous g-C<sub>3</sub>N<sub>4</sub> decorated with cyano groups for photocatalytic hydrogen evolution, *Nanoscale*, 2018, **10**(6), 3008–3013.
- 44 K. N. Kudin, B. Ozbas, H. C. Schniepp, R. K. Prud'homme, I. A. Aksay and R. Car, Raman spectra of graphite oxide and functionalized graphene sheets, *Nano Lett.*, 2008, **8**(1), 36–41.
- 45 J. D. Lee, D. Jishkariani, Y. Zhao, S. Najmr, D. Rosen, J. M. Kikkawa, E. A. Stach and C. B. Murray, Tuning the Electrocatalytic Oxygen Reduction Reaction Activity of Pt-Co Nanocrystals by Cobalt Concentration with Atomic-Scale Understanding, *ACS Appl. Mater. Interfaces*, 2019, **11**(30), 26789–26797.
- 46 K. Sharma, D. Hui, N. H. Kim and J. H. Lee, Facile synthesis of N-doped graphene supported porous cobalt molybdenum oxynitride nanodendrites for the oxygen reduction reaction, *Nanoscale*, 2019, **11**(3), 1205–1216.
- 47 J. Jin, X. Fu, Q. Liu and J. Zhang, A highly active and stable electrocatalyst for the oxygen reduction reaction based on a graphene-supported g-C<sub>3</sub>N<sub>4</sub>@cobalt oxide core-shell hybrid in alkaline solution, *J. Mater. Chem. A*, 2013, **1**(35), 10538.
- 48 J. Chen, X. Yuan, F. Lyu, Q. Zhong, H. Hu, Q. Pan and Q. Zhang, Integrating MXene nanosheets with cobalt-tipped carbon nanotubes for an efficient oxygen reduction reaction, *J. Mater. Chem. A*, 2019, **7**(3), 1281–1286.
- 49 J.-D. Yi, R. Xu, G.-L. Chai, T. Zhang, K. Zang, B. Nan, H. Lin, Y.-L. Liang, J. Lv, J. Luo, R. Si, Y.-B. Huang and R. Cao, Cobalt single-atoms anchored on porphyrinic triazine-based frameworks as bifunctional electrocatalysts for oxygen reduction and hydrogen evolution reactions, *J. Mater. Chem. A*, 2019, **7**(3), 1252–1259.

